Nano Energy 23 (2016) 161–171

Contents lists available at ScienceDirect

Nano Energy

journal homepage: www.elsevier.com/locate/nanoen

Electrochemically modified, robust solid oxide fuel cell anode for direct-hydrocarbon utilization

Yoonseok Choi [a], Evan C. Brown [b,1], Sossina M. Haile [b,*,2], WooChul Jung [a,*]

[a] Department of Materials Science and Engineering, Korea Advanced Institute of Science and Engineering (KAIST), Daejeon 34141, Republic of Korea
[b] Materials Science, California Institute of Technology (Caltech), Pasadena, CA 91125, USA

ARTICLE INFO

Article history:
Received 6 January 2016
Received in revised form
14 March 2016
Accepted 27 March 2016
Available online 30 March 2016

Keywords:
Solid oxide fuel cell anode
Sm-doped ceria
Electrochemical deposition
Coking resistance
Impedance spectroscopy

ABSTRACT

A main advantage of solid oxide fuel cells (SOFCs) operating at a high temperature (> 650 °C) is the flexibility of the fuel they use, specifically as they offer the possibility to utilize methane (natural gas). Unfortunately, however, the state-of-the-art SOFC anodes, composed of a nickel and an anionically conducting oxide such as yttria-stabilized zirconia (YSZ), are associated with Ni-catalyzed carbon deposition and the ensuing degradation of the anode performance. Here, we address these issues through the application of a simple, scalable, cost-effective ceramic coating method known as cathodic electrochemical deposition (CELD). Samaria-doped CeO_2 (SDC) was chosen as the coating material due to its high chemical stability against carbon formation, high electronic and ionic conductivities, and favorable electrocatalytic activity toward fuel oxidation reaction. Nanostructured SDC layers with a high specific surface area were successfully coated onto Ni surfaces via CELD. The physical and chemical attributes of each coating were characterized by a range of analysis tools, in this case SEM, TEM, XRD, EDS, ICP-MS and Raman spectroscopy. An analysis of the AC impedance spectroscopy (ACIS) of Ni-patterned YSZ symmetric cells (anode|electrolyte|anode) with SDC coatings revealed significantly enhanced electrode activity toward fuel oxidation and coking stability under dry or wet methane fuel at 650 °C. These results suggest that the Ni-surface modification via CELD can be a feasible solution for the direct use of hydrocarbon fuels in SOFCs.

© 2016 Elsevier Ltd. All rights reserved.

1. Introduction

Fuel cells are electrochemical devices that convert the chemical energy of fuels directly into electricity with high efficiency, overcoming combustion efficiency limitations (e.g. the Carnot cycle) [1]. Although most fuel cells require hydrogen as a fuel, operation on hydrocarbon fuels, and methane in particular, would enable near-term realization of the efficiency advantages even in the absence of a hydrogen delivery infrastructure. Solid oxide fuel cells (SOFCs) hold promise in this regards, in part because of their relatively high temperature of operation (600–900 °C) [2]. However, the state-of-the-art SOFC anodes, typically cermets composed of nickel and yttria-stabilized zirconia (YSZ), where the former serves as an electronically conducting electrocatalyst and the latter provides the oxygen ion transport pathway, are unsuitable for hydrocarbon electrooxidation because the Ni catalyzes the deposition of graphitic carbon (or "coke"). The deposits not only block access to reaction sites, but also quickly induce mechanical disintegration of the anode [3].

Two key materials strategies have emerged to address the challenge of creating coking resistant SOFC anodes. The first is to replace the Ni with a metal that is catalytically inactive for carbon deposition [4–7], and the second is to replace the entire cermet with a single, mixed ion and electron conducting oxide [8–11]. While both strategies have yielded important successes, neither approach has, as documented in a recent comprehensive review by Ge et al., yielded an SOFC anode with the requisite combination of coking resistance, electrochemical activity and electronic conductivity, to render direct hydrocarbon utilization a technologically attractive proposition [12]. Thus, the field continues to draw considerable attention.

Significantly, the developments to-date hint at future strategies which may bear fruit. In particular, essentially all of the successful demonstrations in the literature of direct hydrocarbon utilization

* Corresponding authors.
E-mail addresses: sossina.haile@northwestern.edu (S.M. Haile), wcjung@kaist.ac.kr (W. Jung).
[1] Present address: Exponent, Inc., 149 Commonwealth Drive, Menlo Park, CA 94025, USA.
[2] Present address: Department of Materials Science and Engineering, Northwestern University, Evanston, IL 60208, USA.

http://dx.doi.org/10.1016/j.nanoen.2016.03.015
2211-2855/© 2016 Elsevier Ltd. All rights reserved.

in SOFCs, where success is defined here as a peak power density exceeding 100 mW cm^{-2} at 700 °C, involve cermet anodes in which ceria, either doped or undoped, is included as a component [4,5,7,9,13–15]. While ceria is typically not considered in the context of the growing discussion of ceramic anodes, several recent observations suggest that it may be the critical component in high activity, coking-resistant systems. First, under the reducing conditions of an SOFC anode, the electronic conductivity of ceria can easily exceed its already high ionic conductivity [16–18]. Second, samaria-doped ceria (SDC) in particular has a high inherent activity for hydrogen electro-oxidation, such that the reaction pathway is dominated by electrocatalysis on the oxide surface with minimal contributions from the oxide-metal-gas triple-phase boundaries (TPBs), even for structures with reaction site densities approaching those of commercial SOFCs [19]. Moreover, by creating nanostructured ceria with high specific surface area, the activity was enhanced by an order of magnitude, again, in the absence of any contribution from catalytically active metals [20]. Third, beyond electrocatalysis, ceria offers tremendous benefits in terms of high temperature stability (with a melt temperature of 2477 °C) and resistance to carbon deposition (oxidation of reduced ceria by CO_2 yields only CO even at conditions in which carbon is the thermodynamically preferred product) [21–23]. Given these attractive features of ceria (and its doped analogs) it is perhaps not surprising that impregnation of metal/YSZ cermet anodes with ceria has shown promise as a route towards effective direct hydrocarbon SOFCs [24–26]. However, the fabrication methods employed to date, to quote Ge, "appear tedious and costly [12]". For example, Yun et al., had to repeat five series of a 24 h dip-coating and 800 °C calcination step to completely cover a Ni/YSZ electrode with SDC [26]. Moreover, little effort appears to have been directed towards the creation of ceria deposits that display high specific surface area so as to take full advantage of the high electrocatalytic activity of the oxide surface [20,27].

Here, we address these issues through the application of a simple, scalable and cost-effective oxide coating method – cathodic electrochemical deposition (CELD). Electrochemical deposition offers many advantages over other oxide deposition methods such as sputtering, chemical vapor deposition, and pulsed laser deposition because it is performed at ambient temperatures and pressures, achieves high growth rates, requires minimal energy input, and is typically carried out in an environmentally benign aqueous solution using relatively simple salt precursors. Furthermore, there are essentially no limits to the area over which material can be deposited, and film morphology can be varied from extremely smooth to extremely rough through control of the wide range of accessible process parameters, with faster growth rates (obtained at high bias or current density) generally leading to rougher films. These features, along with its long history of industrial application, render it a highly cost-effective and tunable technique. In fact, there have been previous studies using CELD to make dense films of ZrO_2, CeO_2, and doped CeO_2, which may be used as an electrolyte material for SOFC [28–31]. Beyond these generic attributes, the distinct mechanism of CELD suggests additional benefits in the context of SOFC electrodes. In contrast to metal electrodeposition, in which a cationic species is reduced to an insoluble metallic form directly on a growing film, oxide precipitation in CELD occurs as a result of electrogeneration of base, a mechanism described in greater detail below. As a consequence, in addition to supporting film growth, the process can generate nanoparticle precipitates within the solution phase. Freedom from the limitation of growth on conductive substrates opens up the intriguing possibility that CELD can be used to coat the surfaces of composite anode structures in which both electronically insulating and electronically conductive phases are present. Indeed, our preliminary studies provide support for this possibility [32], and the present work takes advantage of those initial findings.

To avoid the morphological complexities associated with conventional cermet structures, we employ in the present study model composites comprised of patterned Ni thin-films on YSZ single crystal substrates. After an exploration of deposition conditions, in which deposited materials are examined using a broad range of analytical tools, the electrochemical behavior of the most promising films are evaluated by AC impedance spectroscopy (ACIS). We show that just 1 min of CELD treatment creates an oxide coating that enhances activity for hydrogen electrooxidation relative to the uncoated substrate by a factor of 44, and by almost an order of magnitude in the case of methane. We further show that the CELD coated anode has exceptional resistance to carbon deposition.

2. Material and methods

2.1. Cell preparation

Two types of samples were prepared (see Table 1). In the first type, used for CELD optimization and physical characterization, 300 nm-thick Ni films were deposited on (100) single-crystal Si wafers (10 × 10 × 0.5 mm, Siltron) by DC magnetron sputtering (with a DC power of 100 W, a working pressure of 10 mTorr under a flow rate of 30 sccm Ar, and a deposition rate of 60 nm min^{-1}). The second type of sample was used for electrochemical characterization. Ni electrodes were applied in a symmetric arrangement on both sides of a (100) single crystal YSZ (8 mol%, 10 × 10 × 0.5 mm, MTI Corp.) substrate, which serves as an oxygen-ion conductive electrolyte. The YSZ electrolyte was partially exposed by patterning the 300 nm thick Ni into connected strips in which the Ni width and exposed YSZ width were equal (Table 1 and Fig. S1). Ni patterning was achieved using a photolithographic lift-off process. A positive photoresist (AZ4562) was spin-coated onto the YSZ substrate at 4000 rpm. Next, the samples were aligned by a photomask in a contact aligner and exposed to UV light for 55 s. The Ni layer was sputtered by DC magnetron sputtering with deposition conditions identical to those above. Metal lift-off was achieved by immersing the samples in acetone at room temperature and subjecting them to ultrasonification. Electrochemical measurements were performed using Ni strip widths of 10, 20, 40 and 80 μm, corresponding to triple-phase boundary densities ranging from 85 to 645 cm cm^{-2}. A few additional patterns (of slightly differing geometries) were examined to explore ceria deposition behavior.

2.2. Electrochemical deposition

For both types of samples, SDC layers were applied by CELD using a standard three-electrode system (Fig. 1(a)) comprised of the deposition substrate as the working electrode (held in place using tailor-made aluminum clips), a counter electrode (carbon

Table 1
Two types of samples were prepared in this work. One for CELD optimization and physical characterization (Type 1, Ni|Si substrate) and the other for electrochemical characterization (Type 2, patterned Ni|YSZ substrate|patterned Ni).

Type	Substrate	Name	Ni width [μm]	Ni–Ni distance [μm]	3PB length [cm/cm^2]	2PB area [cm^2/cm^2]
1	Si (100)			No patterns		
2	YSZ (100)	10–10	10	10	644.8	0.32
		20–20	20	20	324.8	0.32
		40–40	40	40	164.8	0.32
		80–80	80	80	84.8	0.32

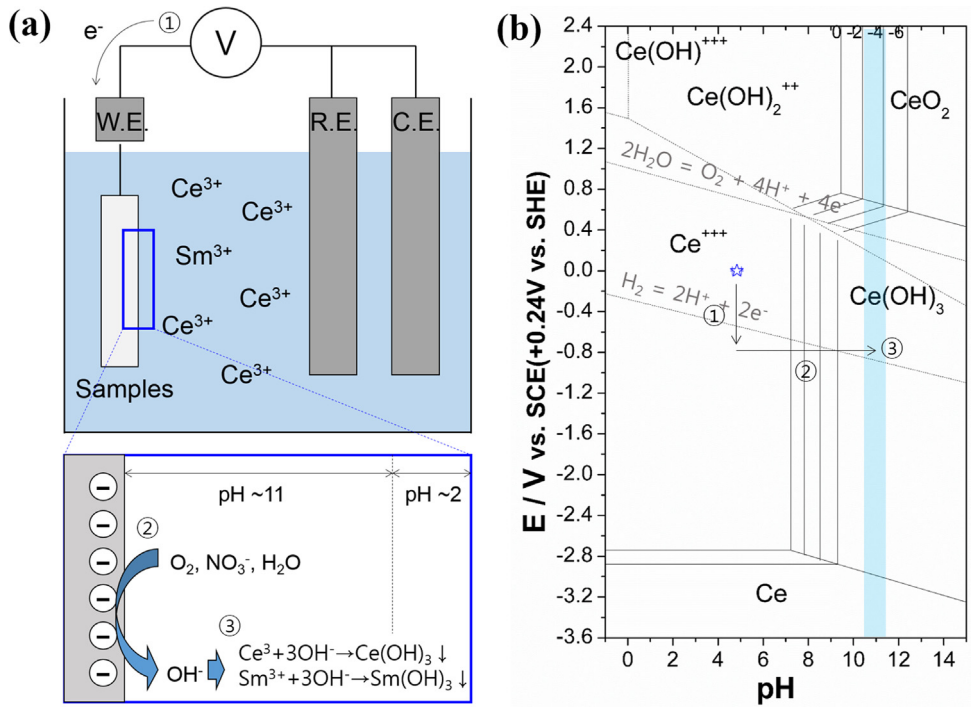

Fig. 1. (a) Schematics of a standard three-electrode system for CELD and SDC growth processes. (b) Pourbaix diagram for Ce–H_2O. (Modified for SCE (+0.24 V vs. standard hydrogen electrode, SHE) from Ref [34]). Highlighted point (blue star) is a starting status of the prepared solution whose pH=4.8 ± 0.2 without the applied potential. The numbers with arrows indicate the serial SDC growth processes.

rod) and a reference electrode (saturated calomel electrode (SCE, +0.24 V vs. SHE), Koslow), all immersed in a solution of 0.05 M $Ce(NO_3)_3 \cdot 6H_2O + Sm(NO_3)_3 \cdot 6H_2O$ (Alfa Aesar, 99.99%) in 60 ml of D.I. water (18.2 MΩ cm, 25 °C). While CELD of ceria has been achieved using chloride salts, residual Cl has been detected in the product oxide [33], motivating the use here of nitrate precursors. Each electrode was carefully positioned while maintaining a constant distance between the other electrodes and a constant depth in the solution.

Electrochemical deposition was conducted in the potentiostat mode, in which the electric potential between the working electrode and reference electrode is controlled while the current response from the counter electrode to the working electrode is measured. Based on a preliminary study [32], several parameters were systematically varied to explore the influence on film morphology, specifically, cathodic potential (primarily in the rage −0.6 to −0.8 V vs. SCE), deposition time (1–60 min), and Sm concentration ($[Sm^{3+}]/[Sm^{3+}+Ce^{3+}]$=0.05, 0.1, 0.15). To ensure reproducibility in the dissolved oxygen content, each solution was stirred for 30 min prior to use in deposition.

2.3. Physical characterization

Film microstructure and thickness were examined by scanning electron microscopy (SEM, Nova 230) and transmission electron microscopy (TEM, 300 kV-Tecnai G2 F30 S-Twin). The chemical composition of the deposits was analyzed using energy dispersive spectrometry (EDS) and inductively coupled plasma mass spectrometry (ICP-MS, Agilent IPC-MS 7700S). For the ICP-MS measurement a mixture of nitric and hydrochloric acid (7:3) was used to dissolve the SDC coating layers at 200 °C for 30 min by microwave digestion to create an analytical reagent. BET measurements (Autosorb-iQ 2ST/MP (Quantachrom Corp.), Kr at 77.3 K) were conducted to evaluate specific surface area. To assure the sensitivity of the technique, identical 5 samples (type 1) with SDC coating layers were prepared. X-ray diffraction (XRD, Rigaku Ultima IV) using Kα(Cu) radiation (40 kV, 40 mA) and Raman spectroscopy (Ar ion CW 514 nm laser, Aramis-Horiba) were conducted to confirm phase formation. In addition, 2-D Raman mapping was performed (ARAMIS, Ar ion CW laser 514.5 nm) to detect possible carbon deposits subsequent to prolonged exposure to CH_4.

2.4. AC impedance spectroscopy

Electrochemical analyses of symmetric cells (Ni|YSZ|Ni) with or without the SDC coating layers were carried out by ACIS (VSP-300, Biologic) under various gas compositions, including hydrogen or methane, over the temperature range of 600–700 °C. AC amplitude of 10 mV was used throughout, after tests had shown that this voltage lies within the linear regime of the sample's current–voltage response. The measurement frequency range was from 0.05 Hz to 7 MHz. The cells were placed inside an alumina tube into which the mixtures of gases (H_2–H_2O–N_2 or CH_4–H_2O) were delivered via digital mass flow controllers (MFCs). Contact to the cells was made using a Pt-Ir clip that firmly held the sample in place and avoided the use of pastes. A pseudo-four-probe configuration was employed to minimize inductance effects from the wiring. The humidity of the gases was controlled by passing them through a D.I. water bubbler immersed in an isothermal bath, the temperature of which was fixed at 10 °C so as to avoid possible water condensation during the measurement. The total gas flow rate was kept fixed at 100 sccm for H_2, implying a gas velocity of 19.7 cm min^{-1} (50 sccm for CH_4, implying a gas velocity of 9.87 cm min^{-1}) throughout the measurements. The real-time humidity was monitored using a humidity sensor (Rotronic Hygroflex).

3. Results and discussion

3.1. Physical and chemical characterization of CELD films

SEM micrographs of the layers grown by CELD on Ni|Si substrates are presented in Fig. 2 showing the influence of applied potential, deposition time, and Sm concentration. The microstructure is formed of a high density collection of upright, interpenetrating nanoscale 'petals', 10–50 nm in thickness, with random in-plane orientation. This morphology has been reported in a handful of previous studies [31,32,34], and appears preferentially at high deposition rate, which, in turn, occurs at large cathodic potential, −0.8 to −0.65 V (Fig. 2(a)–(c)). At −0.6 V, no deposition was observed, a result that may reflect the relatively short deposition time. Elsewhere, dense, planar and very thin ceria films have been obtained under similar potential but longer deposition time [32]. With increasing deposition time at −0.8 V, the film thickness increases (Fig. S3), indicating that despite the insulating nature of the oxide deposit at room temperature, the electrochemical reaction continues. At a film thickness greater than 1 μm, cracks appear (Fig. 2(d)–(f)). Although it is possible that these cracks form directly during film growth, it is more likely that they result from the volume change in transforming from a hydrated cerium oxy-hydroxide to CeO_2 [32,35]. Increasing the Sm dopant concentration in the solution causes the films to become smoother and lose their nanostructured features (Fig. 2(g)–(i)). This observation is in accordance with previous works, which reported the compact "glass-like" morphologies of Gd or Sm doped ceria films [34,36].

While a detailed mechanistic investigation of the CELD process is not the goal of the present work, it is instructive to consider what is known about the mechanism to understand the morphological characteristics of the coatings obtained [37]. A Ce–H_2O Pourbaix diagram representing the thermodynamically stable phases in the potential-pH space is shown in Figure 1(b) [38]. The initial solution pH is 4.8 ± 0.2, placing the system in the region of phase space in which Ce^{3+} occurs as a soluble species. Upon application of cathodic potential, reduction of species such as H_2O, O_2, H^+ or NO_3^- at the working electrode results in an increase in the concentration of hydroxyl ions and hence an easily detected increase in pH [39,40]. The increase in pH drives the system into the region of phase space in which $Ce(OH)_3$ precipitation is expected, and a solid product presumably results. The precise point in the process in which Ce^{3+} is oxidized to Ce^{4+} is unknown. As suggested in the literature, either in solution, particularly when the solution is highly aerated, or during subsequent exposure to

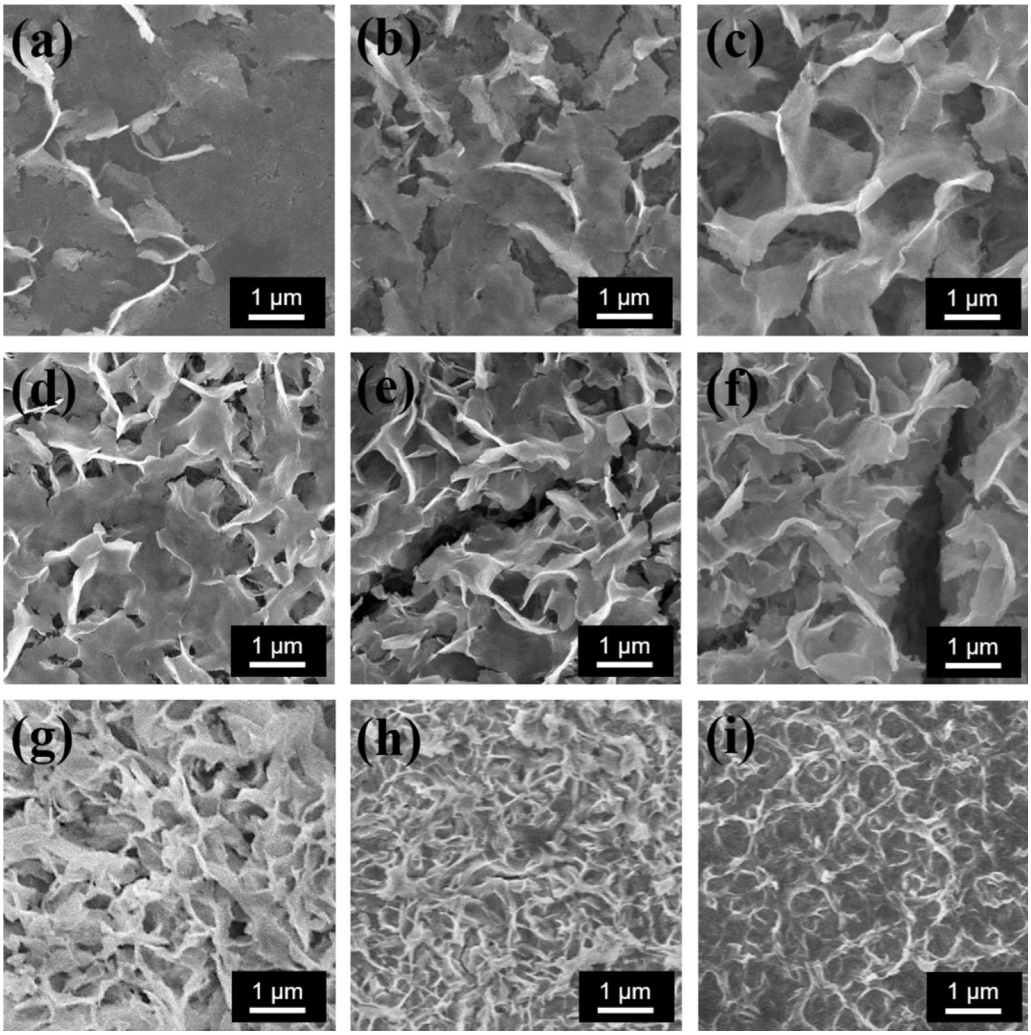

Fig. 2. (a)–(c) SEM images of undoped ceria layers on Ni (on Si), with applied potential (vs. SCE) varying from (a) −0.65 V, (b) −0.7 V to (c) −0.8 V. (Ni|Si substrate/dep. time = 100 s). (d)–(f) SEM images of undoped ceria layers on Ni (on Si), with deposition time varying from (d) 30 s, (e) 60 s to (f) 180 s. (Ni|Si substrate/−0.8 V vs. SCE) (g)–(i) SEM images of doped ceria layers on Ni (on Si) with Sm molar concentration in the initial solutions varying from (g) 5%, (h) 10%, to (i) 15%. (Ni|Si substrate/−0.8 V vs. SCE/dep. time = 100 s).

air, are plausible. The as-deposited material contains substantial concentrations of water and nitrate species [32], which are readily removed in a drying or annealing step, yielding CeO_2 as the final product, as established by X-ray diffraction studies (Fig. 6(a)), and Raman spectroscopy (Fig. S2).

The strong influence of the applied potential on the morphology of the layers grown by CELD, with increasing magnitude in applied potential resulting in a decrease in feature size (Fig. 2(a)–(c)), is likely to be a consequence of diffusion-limited growth kinetics. As the applied potential is made increasingly negative, the current density increases (Fig. S4), implying an increase in film growth rate. At the lowest (least negative) potentials examined, and hence lowest growth rates, the films are relatively smooth and featureless. At high growth rates, encompassing most of the range of voltages examined, metal ions are likely depleted in the vicinity of the surface, and the crystal protrudes towards regions with higher nutrient concentration, ultimately generating the random, porous structures observed [41]. In the case of very negative applied potentials (< -0.8 V, films not shown), hydrogen evolution was detected, with detrimental impact on film adhesion, and a high density of cracks was observed. Accordingly, a deposition bias of -0.8 V, generating the desirable morphology in a short time, along with good film adhesion and an acceptable crack density, was selected for film growth.

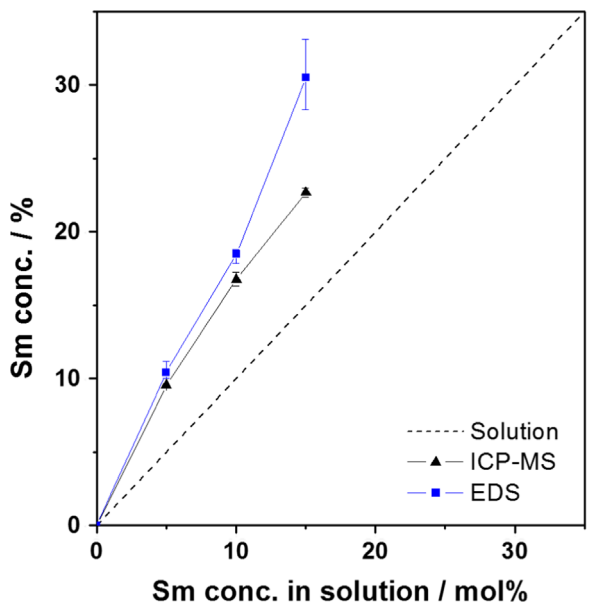

Fig. 3. The results of composition analyses by ICP-MS (▲ black) and EDS (■ blue). (Ni|Si substrate/ -0.8 V vs. SCE/dep. time = 100 s). Error bars in EDS and ICP-MS data represent the distribution in values obtained in four different regions of each sample and three different measurements of each sample, respectively.

The deposition time has no apparent impact on the nanoscale petal morphology. The film thickness increases almost linearly with time at a rate of 20.1 nm sec^{-1} (either doped or undoped, -0.8 V) until approximately 600 s (Fig. S3). Thereafter, the rate of growth gradually decreases, presumably as a result of the increasing coverage of Ni by the non-conducting SDC. However, the decline is limited, suggesting Ni coverage is not complete, and films as thick as 45 μm are obtained after a 1 h deposition. As stated above, thicker films (> 1 μm) obtained after longer growths tend to form large cracks (Fig. 2(d)–(f)), which are likely to be detrimental to charge transport in the SCD layer when utilized as an anode. Accordingly, a deposition time of 60 s (producing films ~1 μm in thickness, Fig. S5) was selected for subsequent electrocatalysis studies.

Fig. 3 presents a comparison of the nominal solution concentration of Sm (as a mole fraction of the total cation content) to the measured concentration of Sm in the film, as determined both by EDS and ICP-MS. Deposition of samaria films by a process similar to that described here for the CELD growth of ceria has been reported [42], and thus it is not surprising that Sm can be incorporated into CELD ceria films. As observed in previous studies, the Sm concentration in the film is substantially higher than that in the solution. This behavior may result from that fact that standard reduction potential of Ce^{3+} is more negative than that of Sm^{3+} [43] or from the fact that $Sm(OH)_3$ has lower solubility than $Ce(OH)_3$ [44]. In addition, the morphology of the deposited SDC layer becomes less nanostructured as the Sm content is increased (Fig. 2(c),(g)–(i)). Hereafter, solutions with 5 mol% Sm were used to obtain films of stoichiometry $Sm_{0.1}Ce_{0.9}O_{1.95-\delta}$, a widely used solid electrolyte composition.

Fig. 4(a)–(c) shows SEM images of CELD ceria deposited over a representative 10 μm Ni pattern on YSZ using the optimal conditions selected above. Not surprisingly, the Ni surfaces are uniformly covered with SDC of the nanoscale petal morphology. More significantly, as proposed, SDC deposition occurs on the YSZ surface, despite the electronically insulating nature of the oxide substrate. The SDC-coated region extends approximately 1–2 μm from the edge of the Ni. Changing the deposition geometry resulted, in some cases, in SDC deposition over the entirety of the exposed YSZ (Fig. S6). The atomic scale features of the YSZ|SDC and

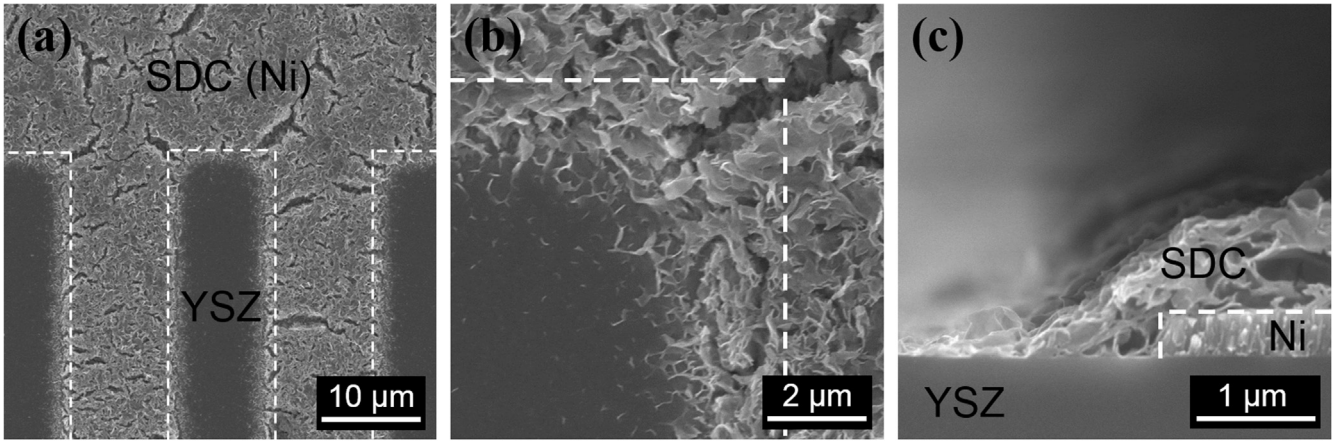

Fig. 4. (a) SEM image of SDC deposited over a representative 10 μm Ni pattern on YSZ using optimal conditions (-0.8 V vs. SCE/5% Sm/dep. time = 60 s) and (b) magnified image near the edge of the patterned Ni. (c) Cross-sectional SEM image of a similar sample. The SDC-coated region extends 1–2 μm from the edge of the Ni (— white dashed line: outline of patterned Ni).

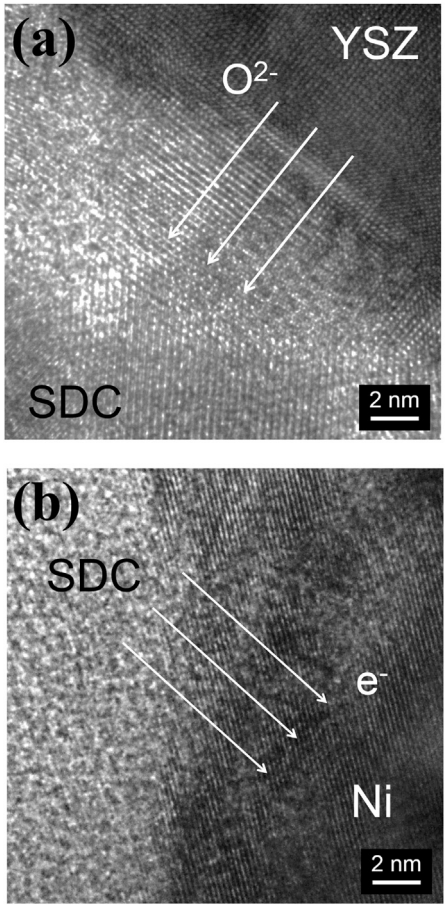

Fig. 5. TEM images of (a) the YSZ|SDC and (b) the Ni|SDC interfaces in a representative sample, showing good contact for easy oxygen ion and electron transfers, respectively.

Ni|SDC interfaces are shown in Fig. 5. The imaged regions indicate good contact, suggesting easy transport of ionic species between the two oxides, Fig. 5(a), and ready electron transport between SDC and Ni, Fig. 5(b). These features are essential for supporting a global electrochemical reaction mechanism that takes advantage of the high reactivity at the SDC|gas interface. It needs to be noted that no interface phase was observed after 85 h of impedance spectroscopy at 700 °C (Fig. S7).

XRD patterns of the as-deposited and annealed samples are presented in Fig. 6(a), for both the undoped and Sm-doped compositions, along with corresponding SEM images. Some discrepancies exist in the literature with regard to the crystal structure of the as-deposited material; both $Ce(OH)_3$ and Ce_2O_3 have been suggested [32,45]. However, the present XRD results show only a cubic fluorite structure, indicating that $CeO_{2-\delta}$ is the primary phase under the deposition conditions used in this work. The lattice constants of the undoped and doped ceria films were calculated as 5.412 Å and 5.425 Å, respectively, which agree well with the reported values of 5.411 Å for pure ceria and 5.423 Å for $Sm_{0.1}Ce_{0.9}O_{1.95}$ [46]. No other phases, such as Sm_2O_3 or $Ce(OH)_3$, are detected. After annealing in dry H_2 for 10 h, the XRD peaks become sharper, indicative of crystallite growth. The crystallite sizes are estimated, according to the Scherrer equation [47], to be 4.6 ± 0.2 nm and 20.1 ± 0.2 nm, respectively for as-deposited and annealed ceria films. However, significantly, the film maintains the high specific surface area of $19 \pm 5\ m^2\ g^{-1}$ upon H_2 annealing at 700 °C for 10 h, compared to as-deposited area of $13 \pm 4\ m^2\ g^{-1}$, measured by BET, and only slight differences are evident between the pre- and post-annealed SEM images (Fig. 6(b) and (c)). Extreme

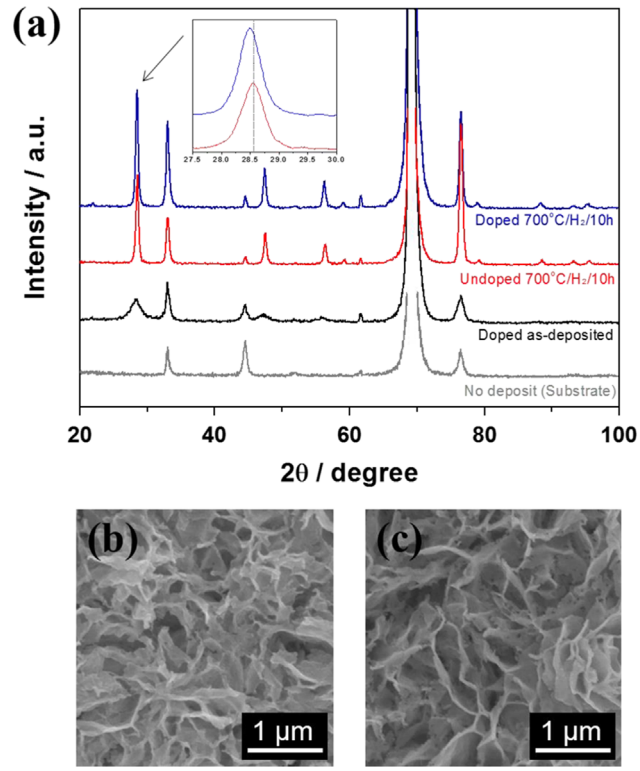

Fig. 6. (a) X-ray diffraction results of Ni|Si substrate (gray), doped ceria layer as-deposited (black), undoped ceria layer after 10 h H_2 annealing at 700 °C (red), and doped ceria layer after 10 h H_2 annealing at 700 °C (blue). (inset: expansion about the peak at ~28.5° of undoped and doped ceria layers) Marks (*) correspond to cubic fluorite structure ($Fm\bar{3}m$ (225)). (b), (c) SEM images of the SDC morphology (b) before (as-deposited) and (c) after 10 h H_2 annealing at 700 °C.

morphological stability of ceria has been previously reported [48]. Furthermore, because no high temperature calcination is required after the CELD step, one can expect such high surface area will be maintained during fuel cell operation. Raman spectroscopy confirms the absence of secondary phases in the as-grown films and the removal of nitrate ions upon annealing (Fig. S2).

3.2. Electrochemical activity

Selected AC impedance results obtained at 650 °C in wet H_2 (0.8% H_2O–10% H_2–N_2) and in wet CH_4 (2% H_2O–98% CH_4) atmosphere are presented in Figs. 7 and 8, respectively. For the cells with bare Ni patterns on YSZ (type 2), the impedance response, plotted in Nyquist form (Fig. 7(a) and (b)), always consists of a nearly ideal semicircle, displaced from the origin by a high-frequency offset resistance (R_{off}). Similar impedance spectra for Ni|YSZ|Ni symmetric systems have been reported elsewhere [49]. The high-frequency offset is attributed to a combination of the ionic resistance of the YSZ and the sheet resistance of the current collector. The arc reflects the characteristics of the electrochemical reaction and is modeled using a *RQ* subcircuit, where *Q* is a constant-phase element with impedance Z_Q equal to $1/Q(i\omega)^n$, *n* is a constant, and ω is the frequency. Consistent with the near-ideal shape of this impedance response, the fitted *n* value was found to fall within the range 0.89–0.91. The capacitance of this response, computed according to $C=(R^{1-n}Q)^{1/n}$, ranges from 10.7 to 11.4 μF cm^{-2} and, within error, is independent of oxygen partial pressure dependence (Fig. 7(c)). Such behavior of the bare Ni is consistent with that of typical double-layer capacitor-type electrodes [50]. Moreover, as shown below, the resistance is found to depend almost linearly on triple-phase boundary length (l_{TPB}). These characteristics are indicative of an electrochemical process occurring at the Ni|YSZ|gas interface.

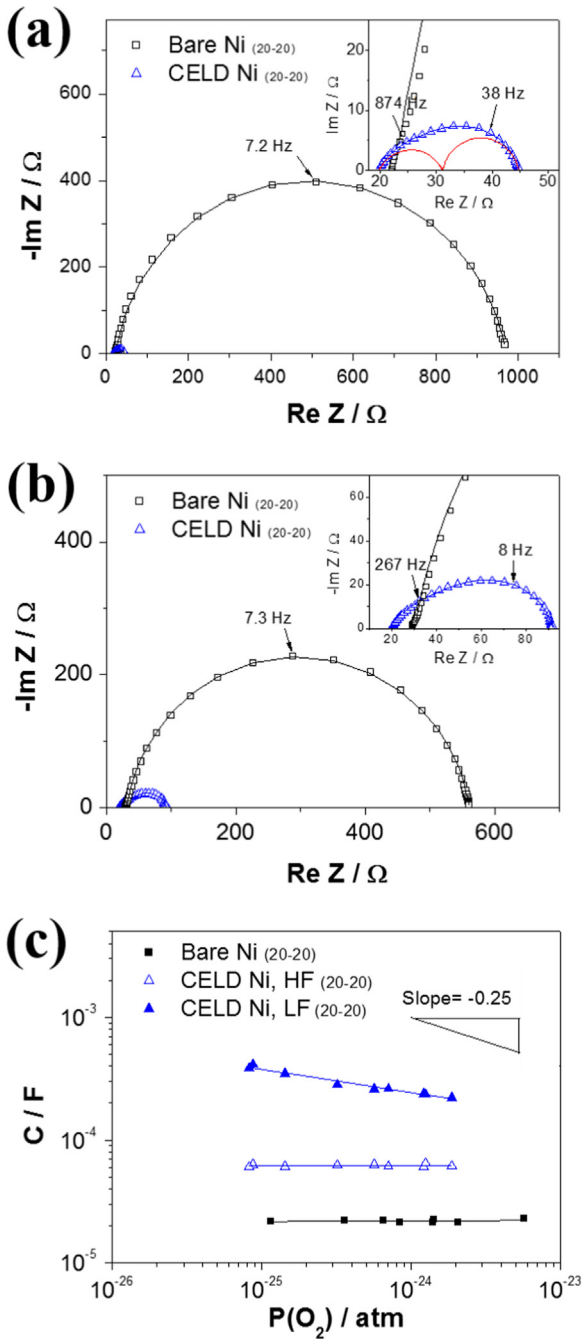

Fig. 7. Typical impedance spectra of Bare Ni (□ black) and CELD Ni (△ blue) of the symmetrical 20–20 patterned Ni|YSZ substrate|patterned Ni anodes and their fitting results (solid lines) (a) under wet H_2 (10% H_2, 0.8% H_2O, N_2 balanced) and (b) under wet CH_4 (98% CH_4, 2% H_2O). (– Red in the inset indicates two distinct arcs in high frequency region (HF) and low frequency region (LF), respectively.) (c) Double logarithmic plots of the capacitance of bare Ni (□) and CELD Ni (▲ LF, △ HF) under vs. pO_2 measured at T=650 °C and pO_2 $\sim 5\times10^{-26}$–5×10^{-24} atm.

In the case of the CELD coated patterns, the near-ideal single arc is replaced with two, highly overlapping arcs (insets in Fig. 7 (a)–(b)) with substantially reduced total resistance, implying that not only has the overall electrochemical reaction pathway been modified, but also that the modification is highly favorable for both hydrogen and methane utilization. In contrast to the electrochemical response, within the range of variations observed in lead-wire ohmic resistance contributions, the offset resistance is unchanged between the two types of electrodes.

In light of the features of the observed spectra, the impedance of the CELD coated patterns was modeled according to an equivalent circuit composed of an offset resistance in series with two serially connected (parallel) *RQ* subcircuits.

The physical origin of these two arcs is not entirely clear. The large capacitance values associated with the lower frequency arc, ranging from 0.118 to 0.208 mF cm^{-2} (normalized relative to the electrolyte projected area), as well as the oxygen partial pressure of this capacitance, with a slope of $\sim -¼$ in the double logarithmic plot, Fig. 7(c), indicates this term is dominated by the chemical capacitance of the deposited ceria [51,52]. Doped ceria behaves as a mixed conductor under the reducing conditions of the measurement and the chemical capacitance results from changes in oxygen content in response to the applied electrical potential perturbation [18]. The surface electrochemical reaction, specifically, hydrogen electrooxidation, has been shown elsewhere to occur in parallel with this capacitance [19], suggesting that the resistance of the low frequency impedance arc corresponds to that of the electrochemical reaction. The high frequency response may be due to constriction effects ensuing from the tortuous electron pathway from surface reaction sites to the embedded metal current collectors or the similarly tortuous ion pathway from the surface reaction sites to the YSZ electrolyte. Such effects have been observed in related measurement configurations [27,32], but have not been confirmed for the present case.

The dependence of the resistance terms of both types of electrodes on l_{TPB}, temperature and gas phase composition, as measured under H_2, is summarized in Fig. 8. As already noted in the context of the raw impedance data, application of the ceria CELD coating dramatically lowers the electrode resistance, even upon comparing the sum of the two resistances from the latter films with the single resistance from the former. The properties of the bare Ni electrodes are similar to those reported in the literature. Not only is the impedance approximately linearly dependent on l_{TPB}, with a power law exponent of -1.47, the absolute value of the length-specific electrode impedance, 1–2 kΩ m at 650 °C is similar to that reported by Bieberle et al. [50] In addition, the dependence on hydrogen partial pressure is negligible, with a power-law exponent of -0.1 (Fig. 8(c)), the dependence on steam partial pressure is considerable, with a power-law exponent of -0.57 (Fig. 8(d)) and the activation energy at fixed gas composition is 0.98 eV (Fig. 8(b)). Again, such characteristics are typical of Ni patterned electrodes on YSZ [49].

Beyond the substantial decrease in electrode resistance upon application of the SDC coating, a significant feature of the results in Fig. 8 is the retention of a strong dependence of the resistance terms on l_{TPB}. Elsewhere we have shown that for patterns on flat ceria surfaces with fixed fractional area of the oxide|gas interface, varied l_{TPB} has no impact (within the range of geometries explored) on the overall electrochemical response [19]. It was further shown that, as a result of the high reaction rate at the SDC|gas interface, the electrochemical reaction occurs predominantly via this double-phase boundary, with negligible contribution from triple-phase boundaries. At first glance, a dependence on l_{TPB} as observed here might be considered incompatible with a reaction that proceeds primarily via the double-phase boundary. However, in light of the preferential SDC deposition on the Ni pattern and thus the limited extent to which the YSZ becomes coated, a dependence on l_{TPB} is not surprising. The structure resulting from the CELD process, Fig. 4, in fact suggests that the SDC in the near vicinity of the YSZ|Ni|SDC triple-phase boundary will be most active. Thus, even where ceria is the active component, the overall activity will scale with the length of the YSZ|Ni|SDC contacts.

That the electrochemical reaction pathway is mechanistically distinct between the bare Ni and the CELD SDC coated Ni is evident from the very different pH_2O, pH_2 and T dependences of the

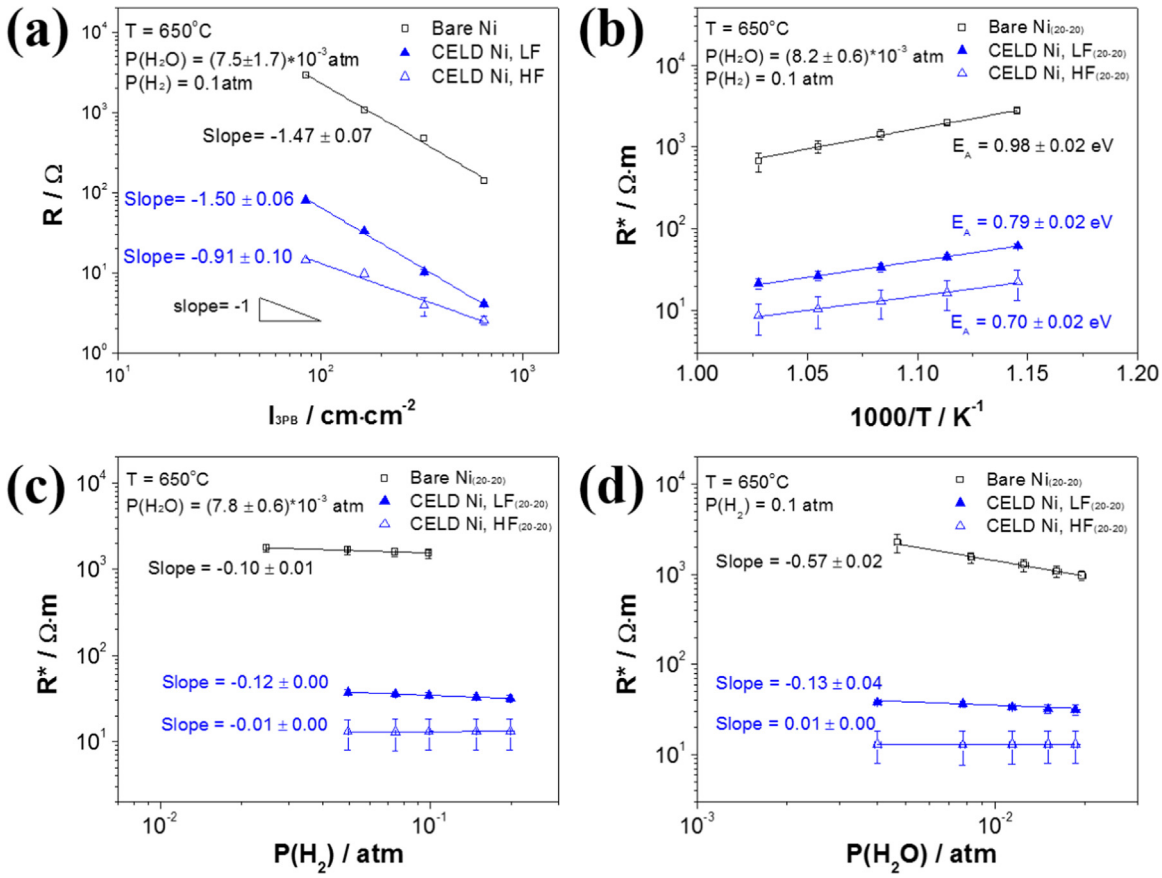

Fig. 8. (a) Double logarithmic plots of the electrode resistances of bare Ni (□ black) and CELD Ni (▲ LF, △ HF blue) vs. 3PB lengths (10–10/20–20/40–40/80–80) under $pH_2 = 0.1$ atm, $pH_2O = (7.5 \pm 1.7) \times 10^{-3}$ atm at $T = 650$ °C. (b) Temperature dependence of the electrode resistance normalized by l_{3PB} (R^*) of bare Ni (□) and CELD Ni (▲ LF, △ HF) under wet H_2 measured at $T = 600$–700 °C. (c) Double logarithmic plots of the R^* of Bare Ni (□) and CELD Ni (▲ LF, △ HF) vs. pH_2 measured at $T = 650$ °C and $pH_2 = 0.02$–0.2 atm, $pH_2O = (7.8 \pm 0.6) \times 10^{-3}$ atm. (d) Double logarithmic plots of the R^* of bare Ni (□) and CELD Ni (▲ LF, △ HF) under vs. pH_2O measured at $T = 650$ °C and $pH_2O = 0.005$–0.019 atm, $pH_2 = 0.1$ atm.

two types of electrodes. In contrast to the behavior of the bare Ni electrodes, the gas composition has negligible influence on the high frequency resistance of the latter (Fig. 8(c) and (d)), supporting the proposal that this response is due to a geometric constriction effect rather than a chemical step in the reaction pathway. The low frequency resistance, on the other hand, displays gas composition dependences and activation energy that are comparable to that observed earlier for porous SDC grown by pulsed laser deposition [20]. Specifically, in that prior study we observed a power law exponent for pH_2 of -0.09, and an activation energy of 0.80 eV. For the low frequency resistance of the CELD films, the respective values are -0.12 and 0.79 eV. From the totality of these observations we conclude that the low frequency response (alone) reflects the true electrochemical reaction resistance, that the reaction proceeds via the SDC|gas interface, and that much of the surface of the CELD SDC may not be utilized because of the challenge of transporting electronic and ionic current through geometrically constricted interfaces. Significantly, under comparable conditions ($T = 650$ °C, $pH_2 = 0.1$ atm, $pH_2O = 0.005$ atm) the previously investigated columnar PLD films yielded an electrolyte-area normalized low-frequency resistance of $\sim 2\ \Omega\ cm^2$ for a film thickness of 2.55 μm [20], whereas the 1 μm thick CELD films display a value only slightly higher, $\sim 3\ \Omega\ cm^2$. The high specific surface area of the CELD films, ~ 13–$19\ m^2\ g^{-1}$ vs. 15–$20\ m^2\ g^{-1}$ for the PLD may explain, in part, the comparable improvement of activities despite the lesser quantity of ceria present in the CELD films. In addition, because low temperature solution based synthesis tends to exclude impurities due to low solubility at the synthesis temperature, it is

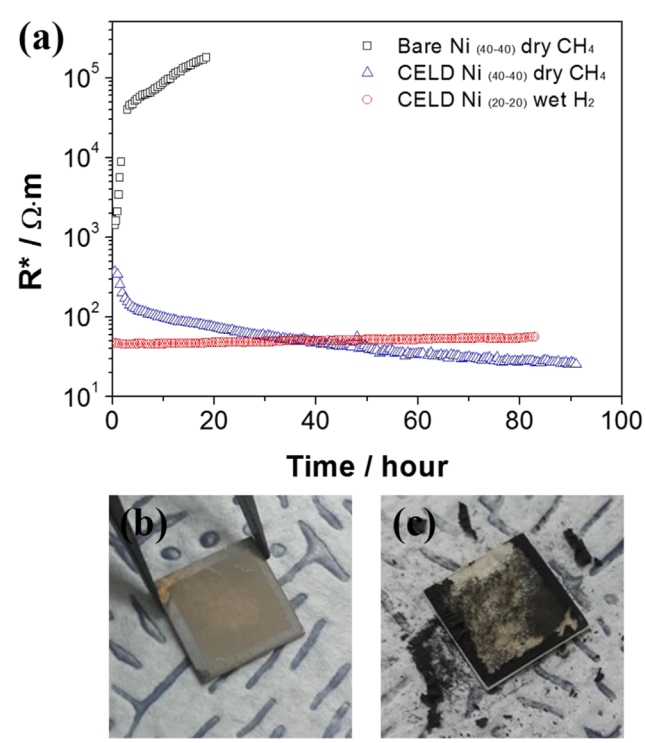

Fig. 9. (a) Temporal evolution of electrode resistance, R^*_{total} ($R^*_{HF} + R^*_{LF}$). Bare Ni (□ black) and SDC coated Ni (△ blue) under dry CH_4 at 700 °C and SDC coated Ni (○ red) under wet H_2 at 700 °C. (b),(c) Optical images of SDC coated Ni and bare Ni electrodes after the long-term electrochemical evaluation under dry CH_4 at 700 °C of part (a).

possible that higher purity in the CELD film has contributed to its low impedance. Efforts are underway to understand these differences and optimize the deposition architecture so as to take full advantage of the enhancements offered by CELD and ideally eliminate the high frequency impedance response.

3.3. Coking resistance

As shown in the raw impedance spectra, application of the SDC CELD coating substantially decreases the fuel electrochemical reaction resistance, by a factor of 44 for hydrogen and a factor of 8 for methane under the specific conditions represented. Under different conditions (not shown) even larger differences between bare and coated films were recorded. Of potentially greater importance than initial performance, particularly for a nanostructured component that will be utilized at high temperature for long periods, is the retention of activity during prolonged exposure to operational conditions. In Fig. 9 is presented a comparison of the length-specific electrochemical reaction resistances of bare and CELD ceria coated Ni-patterned electrodes, upon continuous exposure for tens of hours at 700 °C to dry methane, a particularly demanding condition. In the case of the CELD electrode, results obtained upon exposure to humid H_2 ($pH_2O=0.02$ atm) are additionally reported. For the CELD films, the resistance is taken as the sum of the resistance contributions from the low and high frequency impedance arcs discussed above. The stability of the CELD coated Ni is exceptional. Whereas the bare Ni showed a dramatic, more than two orders of magnitude increase in electrode resistance within three hours and finally lost electrical contact after about 19 h, the CELD films displayed either an almost constant (H_2) or decreasing (CH_4) resistance over time. The tremendous difference between the bare Ni and CELD coated Ni electrodes is further evident in the optical images presented in Fig. 9(b) and (c). The coated film reveals no discernable sign of carbon deposition and only slight morphological changes (Fig. S8) after prolonged exposure to dry methane, whereas in the absence of CELD ceria, carbon is deposited throughout the system and the Ni is no longer visible.

The precise global electrochemical reaction that occurs under dry CH_4 is unclear. In the case of H_2/H_2O, the reaction is easily recognized as

$$H_2+O^{2-}\leftrightarrow H_2O+2e^- \quad (1)$$

with all relevant gaseous species being actively supplied and their concentrations controlled. In the case of dry methane, the equivalent reaction

$$CH_4+3O^{2-}\leftrightarrow CO+2H_2O+6e^- \quad (2)$$

has less meaning because CO and H_2O, although they may be generated locally, are not actively supplied. In light of this

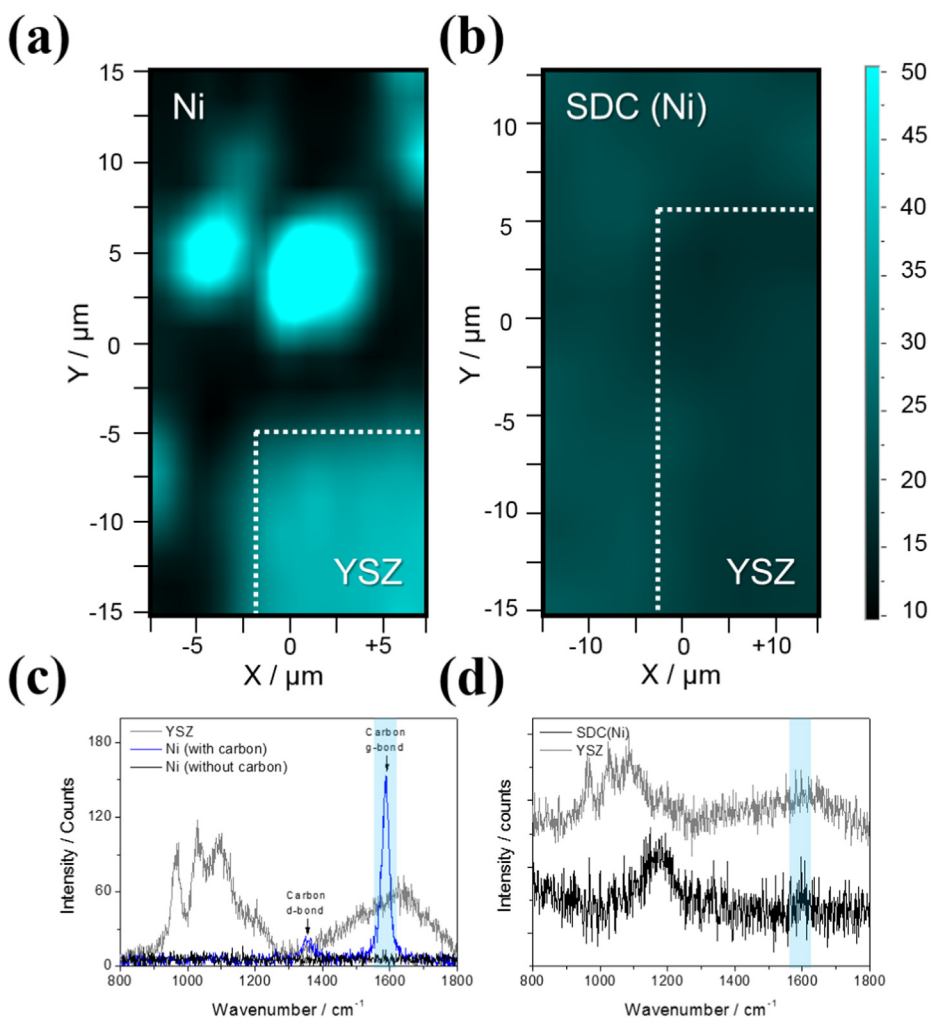

Fig. 10. Raman 2D mapping images after 100 h of measurement under wet CH_4 (98% CH_4, 2% H_2O) at 700 °C from (a) Bare Ni and (b) SDC coated Ni, respectively. Raman spectra obtained from (c) the bare Ni and (d) the SDC coated Ni, respectively. Carbon peaks at ~1350 cm^{-1} for D-band and ~1580 cm^{-1} for g-band. The mapping images were obtained using the g-band region, highlighted in blue in (c)–(d).

uncertainty and the significant performance increase over time, it is of value to consider to what extent oxygen release from the ceria as a result of direct chemical reaction with methane can impact the electrochemical process. If the equivalent pO_2 of pure methane at 700 °C is 10^{-28} atm, referring to the thermogravimetric results of Bishop et al. [53], the expected δ in $Gd_{0.1}Ce_{0.9}O_{1.95-\delta}$ under these conditions is 0.334 and the conductivity is $\sim$2.5 S cm^{-1}, about 7 times higher than the ionic conductivity alone [54]. Given the very small amount of ceria in the CELD electrodes and the high methane flow rate, enough methane is supplied in less than 1 s to achieve δ=0.334 (even assuming an initial δ of 0). As the reaction with methane is likely to be surface reaction limited and only a portion of the reactant gas will interact with the oxide, the actual reduction is likely to take substantially longer than 1 s. Thus, increased electronic conductivity with increasing time of exposure to CH_4 may contribute to the decrease in electrode impedance over time. In addition, a small amount of carbon deposition, which would be expected to occur over a longer time scale than the ceria reduction, may also contribute, particularly to continued performance improvements after tens of hours of exposure. Similar observations were reported by McIntosh et al. using n-butane and the increased activity was similarly attributed to slight carbon deposition that increased electronic conductivity [14,55]. The slight decrease in performance observed in the case of hydrogen electro-oxidation is tentatively attributed to a slight loss in surface area over time, as shown by the slight growth in diffraction feature size upon annealing (Fig. 6a).

The impact of long time exposure to methane is further explored by comparison of Raman spectra of the two types of electrodes, Fig. 10, before and after 100 h of exposure to methane. In this case the gas is humidified so as to represent a more realistic operation condition for direct methane SOFCs, in contrast to the extreme condition of dry methane examined electrochemically. The Raman 2D mapping images are generated using the summed intensities of the carbon D-band (1350 cm^{-1}) and g-band (1580 cm^{-1}) peaks. The bare Ni has regions several microns on edge with a significant carbon signal. Deposition of carbon on the YSZ is not detectable due to the overlap in Raman signals between YSZ and carbon. In contrast to the bare Ni electrode, the CELD SDC coated Ni is entirely free of carbon within the noise level of the measurement. The data provide conclusive evidence that the CELD SDC prevents carbon deposition on Ni. These results are consistent with other reports suggesting high tolerance of ceria to carbon coking [7,19,22,25–27,56,57].

4. Conclusions

Nanostructured SDC was successfully deposited onto Ni by means of a simple, cost-effective CELD method. The SDC layer had an extremely high surface area with good thermal stability up to 700 °C. Lithographically patterned Ni|YSZ model electrodes showed a dramatic increase (by a factor of almost 50) in electrode activity upon application of the CELD coating, consistent with an electrochemical reaction that occurs directly on the SDC surface by a pathway shown schematically in Fig. 11. The dependence of electrode activity of the CELD coated Ni on triple phase boundary length is attributed to enhanced activity of the SDC deposited in the near-vicinity of the Ni|YSZ contact line; SDC deposition over YSZ is limited, whereas SDC deposited over Ni far from the contact line is not well connected to the electrolyte. Despite the imperfect deposition configuration, CELD films just 1 μm thick, requiring a deposition time of just 1 min, provide activity comparable to nanostructured, porous PLD films 2.55 μm thick, which require a deposition time of 125 min without considering additional pumping and heating/cooling time. The attractive performance of the CELD SDC is attributed to the extremely high surface area and potentially low impurity concentration due to

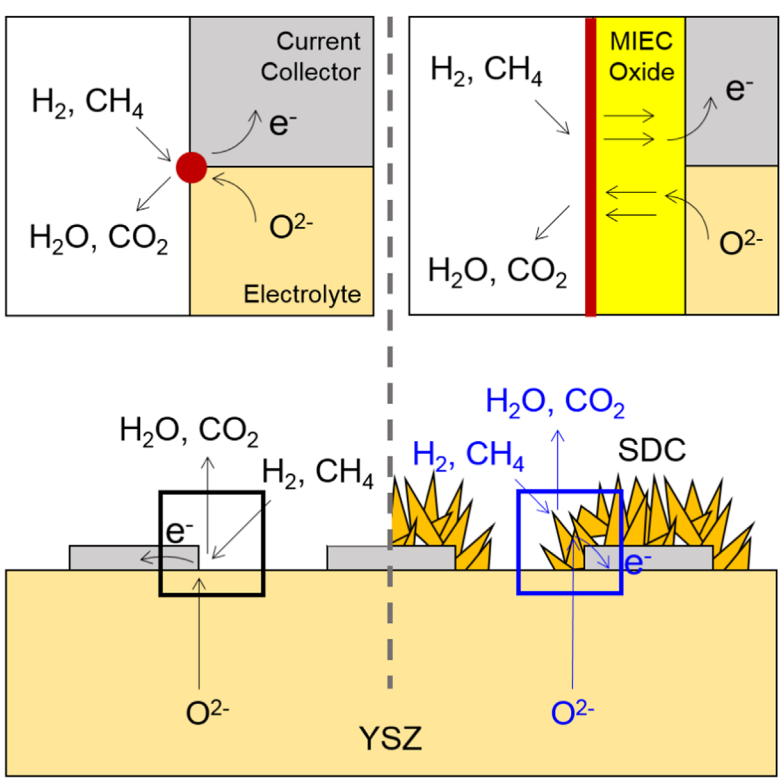

Fig. 11. Schematic illustration of distinct reaction pathways for bare Ni (left) and SDC coated Ni (right) electrodes. Red-highlighted regions are reaction sites for fuel electrooxidation. After CELD coating of SDC on Ni surface, the available reaction sites are understood to expand from 3PB (Ni-YSZ-gas) to 2PB (SDC-gas) sites.

the low temperature synthesis. In addition, the high surface-area CELD SDC effectively prevented carbon coking under both dry and wet (2% H_2O) methane at 700 °C. Thus, the CELD method may provide a highly advantageous route, in terms of both performance and manufacturability, for achieving ultra-high performance SOFCs operating either on hydrogen or directly on methane.

Acknowledgment

This work was supported by the Global Frontier R&D Program on Center for Multiscale Energy System funded by the National Research Foundation under the Ministry of Science, ICT & Future, Korea (2011-0031569). Additional support was provided by the National Research Foundation of Korea (NRF) Grant funded by the Korean Government (MSIP) (No. 2014R1A1A1003008). Preliminary experiments were conducted under financial support of the Global Climate and Energy Program (GCEP) administered by Stanford University, United States (26698940-50708-A).

Appendix A. Supplementary material

Supplementary data associated with this article can be found in the online version at http://dx.doi.org/10.1016/j.nanoen.2016.03.015.

References

[1] Fuel Cell Handbook, EG&G Technical Services, Inc., 2004.
[2] N.Q. Minh, J. Am. Ceram. Soc. 76 (1993) 563–588.
[3] S. McIntosh, R.J. Gorte, Chem. Rev. 104 (2004) 4845–4865.
[4] R.J. Gorte, S. Park, J.M. Vohs, C.H. Wang, Adv. Mater. 12 (2000) 1465–1469.
[5] H. Kan, H. Lee, Catal. Commun. 12 (2010) 36–39.
[6] E. Nikolla, J. Schwank, S. Linic, J. Am. Chem. Soc. 131 (2009) 2747–2754.
[7] S.D. Park, J.M. Vohs, R.J. Gorte, Nature 404 (2000) 265–267.
[8] Y.H. Huang, R.I. Dass, Z.L. Xing, J.B. Goodenough, Science 312 (2006) 254–257.
[9] S. Sengodan, S. Choi, A. Jun, T.H. Shin, Y.W. Ju, H.Y. Jeong, J. Shin, J.T.S. Irvine, G. Kim, Nat. Mater. 14 (2015) 205–209.
[10] S.W. Tao, J.T.S. Irvine, Nat. Mater. 2 (2003) 320–323.
[11] C. Yang, J. Li, Y. Lin, J. Liu, F. Chen, M. Liu, Nano Energy 11 (2015) 704–710.
[12] X.M. Ge, S.H. Chan, Q.L. Liu, Q. Sun, Adv. Energy Mater. 2 (2012) 1156–1181.
[13] T. Hibino, A. Hashimoto, M. Yano, M. Suzuki, M. Sano, Electrochim. Acta 48 (2003) 2531–2537.
[14] S. McIntosh, J.M. Vohs, R.J. Gorte, J. Electrochem. Soc. 150 (2003) A470–A476.
[15] K. Wang, R. Ran, Z.P. Shao, J. Power Sources 170 (2007) 251–258.
[16] H.L. Tuller, A.S. Nowick, J. Phys. Chem. Solids 38 (1977) 859–867.
[17] K. Eguchi, T. Setoguchi, T. Inoue, H. Arai, Solid State Ion. 52 (1992) 165–172.
[18] W. Lai, S.M. Haile, J. Am. Ceram. Soc. 88 (2005) 2979–2997.
[19] W.C. Chueh, Y. Hao, W. Jung, S.M. Haile, Nat. Mater. 11 (2012) 155–161.
[20] W. Jung, J.O. Dereux, W.C. Chueh, Y. Hao, S.M. Haile, Energy Environ. Sci. 5 (2012) 8682–8689.
[21] Synthesis of Lanthanide and Actinide Compounds, Kluwer Academic Publishers, 1991.
[22] O.A. Marina, C. Bagger, S. Primdahl, M. Mogensen, Solid State Ion. 123 (1999) 199–208.
[23] W.C. Chueh, S.M. Haile, ChemSusChem 2 (2009) 735–739.
[24] T. Suzuki, T. Yamaguchi, K. Hamamoto, Y. Fujishiro, M. Awano, N. Sammes, Energy Environ. Sci. 4 (2011) 940–943.
[25] W. Zhu, C. Xia, J. Fan, R. Peng, G. Meng, J. Power Sources 160 (2) (2006) 897–902.
[26] J.W. Yun, H.C. Ham, H.S. Kim, S.A. Song, S.W. Nam, S.P. Yoon, J. Electrochem. Soc. 160 (2013) F153–F161.
[27] W. Jung, K.L. Gu, Y. Choi, S.M. Haile, Energy Environ. Sci. 7 (2014) 1685–1692.
[28] L. Gal-Or, A. Kohn, H.W. Hennicke, J. Electrochem. Soc. 138 (7) (1991) 1939–1942.
[29] I. Zhitomirsky, A. Petric, Mater. Lett. 50 (4) (2001) 189–193.
[30] E.A. Kulp, S.J. Limmer, E.W. Bohannan, J.A. Switzer, Solid State Ion. 178 (2007) 749–757.
[31] K. Kamada, N. Enomoto, J. Hojo, Electrochim. Acta 54 (2009) 6996–7000.
[32] E. C. Brown, Ph.D thesis, Caltech, 2011.
[33] I. Zhitomirsky, J. Eur. Ceram. Soc. 19 (15) (1999) 2581–2587.
[34] L. Zivkovic, V. Lair, O. Lupan, A. Ringuede, Thin Solid Films 519 (2011) 3538–3543.
[35] I. Zhitomirsky, A. Petric, Ceram. Int. 27 (2001) 149–155.
[36] O.S. Khalipova, V. Lair, A. Ringuede, Electrochim. Acta 116 (2014) 183–187.
[37] I. Zhitomirsky, Adv. Colloid Interface Sci. 97 (2002) 279–317.
[38] M. Pourbaix, Atlas of Electrochemical Equlibria in Aqueous Solutions, Pergamon Press Ltd, New York, 1966, First English ed..
[39] Y.C. Zhou, J.A. Switzer, J. Alloy. Compd. 237 (1996) 1–5.
[40] L. Yang, X. Pang, G. Fox-Rabinovich, S. Veldhuis, I. Zhitomirsky, Surf. Coat. Technol. 206 (2011) 1–7.
[41] M.J. Siegfried, K.S. Choi, Angew. Chem. Int. Ed. 47 (2008) 368–372.
[42] E.J. Ruiz, R. Ortega-Borges, L.A. Godinez, T.W. Chapman, Y. Meas-Vong, Electrochim. Acta 52 (2006) 914–920.
[43] CRC Handbook of Chemistry and Physics, CRC Press, 87 ed., 2006.
[44] T. Moeller, H.E. Kremers, J. Phys. Chem. B 48 (1944) 395–406.
[45] P. Bocchetta, M. Santamaria, F. Di Quarto, J. Appl. Electrochem. 39 (2009) 2073–2081.
[46] G. Brauder, H. Gradinger, Z. Anorg. Allg. Chem. 276 (1954) 209–226.
[47] P. Scherrer, Gött. Nachr. Gesell 2 (1918) 98.
[48] W.C. Chueh, C. Falter, M. Abbott, D. Scipio, P. Furler, S.M. Haile, A. Steinfeld, Science 330 (2010) 1797–1801.
[49] W.G. Bessler, M. Vogler, H. Stoermer, D. Gerthsen, A. Utz, A. Weber, E. Ivers-Tiffee, Phys. Chem. Chem. Phys. 12 (2010) 13888–13903.
[50] A. Bieberle, L.P. Meier, L.J. Gauckler, J. Electrochem. Soc. 148 (2001) A646–A656.
[51] W.C. Chueh, S.M. Haile, Phys. Chem. Chem. Phys. 11 (2009) 8144–8148.
[52] C. Chen, D. Chen, W.C. Chueh, F. Ciucci, Phys. Chem. Chem. Phys. 16 (2014) 11573–11583.
[53] S.R. Bishop, Acta Mech. Sin. 29 (2013) 312–317.
[54] S.R. Wang, T. Kobayashi, M. Dokiya, T. Hashimoto, J. Electrochem. Soc. 147 (2000) 3606–3609.
[55] S. McIntosh, H.P. He, S.I. Lee, O. Costa-Nunes, V.V. Krishnan, J.M. Vohs, R.J. Gorte, J. Electrochem. Soc. 151 (2004) A604–A608.
[56] E.P. Murray, T. Tsai, S.A. Barnett, Nature 400 (1999) 649–651.
[57] J. Qiao, N. Zhang, Z. Wang, Y. Mao, K. Sun, Y. Yuan, Fuel Cells 9 (2009) 729–739.

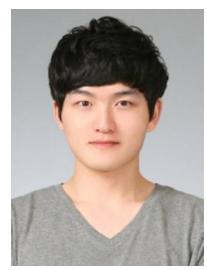

Yoonseok Choi is a Ph.D. student in the department of Materials Science and Engineering (MSE) at Korean Advanced Institute of Science and Technology (KAIST) in Daejeon. He received his Bachelor's degree in the department of MSE from Hanyang University in Seoul and completed his Master's degree in 2015 in the department of MSE at KAIST on the development solid oxide fuel cell (SOFC) anodes for direct-hydrocarbon utilization using electrochemical deposition. His current research is about ceria-based anodes for SOFCs.

Evan C. Brown is a Principal Engineer at Exponent, a scientific and engineering consulting firm, where he assists clients in a variety of materials science related topics, primarily in consumer electronics applications. Previous to working at Exponent, he earned his Ph.D. in Materials Science and Engineering from the California Institute of Technology in 2011, for investigations of solid oxide fuel cell fabrication techniques.

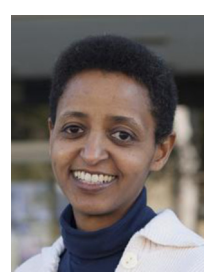

Sossina M. Haile is the Walter P. Murphy Professor of Materials Science and Engineering at Northwestern University, a position she assumed in 2015 after serving 18 years on the faculty at the California Institute of Technology. She earned her Ph.D. in Materials Science and Engineering from the Massachusetts Institute of Technology in 1992, after which she was appointed a Humboldt Post-Doctoral Fellow at the Max Planck Institute for Solid State Research in Stuttgart, Germany. Haile's research broadly encompasses solid state electrochemical materials and devices, with particular focus on energy technologies.

WooChul Jung received his Ph.D. degree in Materials Science and Engineering from Massachusetts Institute of Technology (MIT) and served as postdoctoral fellow in Materials Science at California Institute of Technology (Caltech). He is now an assistant professor of the department of MSE at Korea Advanced Institute of Science and Technology (KAIST). His research emphasizes the characterization and optimization of interface reaction kinetics between gases and ionic solids for applications in solid oxide fuel cells, electrolyzers and gas permeation membranes.